In situ growth route towards anti-perovskite Ni$_3$InN nanoparticles embedded within amorphous silicon nitride

Journal:	*Journal of Materials Chemistry A*
Manuscript ID	TA-ART-10-2023-006212.R1
Article Type:	Paper
Date Submitted by the Author:	06-Dec-2023
Complete List of Authors:	Tada, Shotaro; Indian Institute of Technology Madras, Department of Metallurgy and Materials Engineering; Nagoya Institute of Technology, Department of Life Science and Applied Chemistry, Graduate School of Engineering Takazawa, Sakurako; Nagoya Institute of Technology, Department of Life Science and Applied Chemistry, Graduate School of Engineering Asakuma, Norifumi; Nagoya Institute of Technology, Department of Life Science and Applied Chemistry, Graduate School of Engineering Cheype, Maxime; Université de Limoges Honda, Sawao; Nagoya Institute of Technology, Kumar, Ravi; Indian Institute of Technology Madras, Bernard, Samuel; CNRS, Research Institute on Ceramics Iwamoto, Yuji; Nagoya Insittute of Technology,

ARTICLE

In situ growth route towards anti-perovskite Ni₃InN nanoparticles embedded within amorphous silicon nitride

Shotaro Tada,[a, d] Sakurako Takazawa,[a] Norifumi Asakuma,[a] Maxime Cheype,[b] Sawao Honda,[a] Ravi Kumar[c], Samuel Bernard,[b] and Yuji Iwamoto*[a]

Herein, we report a new approach toward the design of anti-perovskite nitrides at nanoscale. This study deals with a precursor route to *in situ* grow anti-perovskite nickel indium nitride (Ni₃InN) nanoparticles (NPs) in an amorphous silicon nitride (a-SiN). Precursors are synthesized via the modification of polysilazanes (PSZs) by controlled amounts of nickel (NiCl₂) and indium (InCl₃) chlorides. Subsequently, as-synthesized precursors are pyrolyzed in the temperature range of 300–600 °C in flowing ammonia (NH₃) to afford Ni₃InN/a-SiN nanocomposites. The single-step process is discussed based on a complete set of characterization techniques, including elemental analyses, X-ray diffraction (XRD), thermogravimetric-mass spectrometric (TG-MS) analyses, infrared and X-ray photoelectron spectroscopies, and transmission electron microscopy (TEM) observations. It has been demonstrated that the synthesis of precursors proceeded via the prior formation of Ni NPs at 300 °C before the subsequent migration of In species, which governs the *in situ* formation of the nanoscale anti-perovskite Ni₃InN phase in the matrix. As a proof of concept, we investigated CO₂ adsorption-desorption capabilities of this new type of self-supported nanocatalysts.

Introduction

Transition metal (M) nitrides (MN) have received significant attention as promising and sustainable substitutes for noble metals in catalyst-assisted reactions.[1–3] In this category, anti-perovskite nitrides—antiperovskites are similar in crystal structure to perovskites but have an inverted electrical configuration—stand out as an advanced material with distinctive functionalities such as negative magnetocaloric effect,[4–6] negative thermal expansion,[7,8] ionic conductivity[9,10] and superconductivity.[11–13] Recently, these nitrides demonstrated catalytic properties, particularly as nitrogen storage agents for chemical looping ammonia (NH₃) production,[15,16] and in the electro-reduction of carbon dioxide.[17]

Typically, anti-perovskite compounds are synthesized through solid-state reactions involving the appropriate parental compounds, which usually proceed around their melting point. Alternate methods like direct or carbothermal nitridation of

intermetallic or oxide precursors are also employed.[15] However, due to huge challenges in controlling their synthesis at nanoscale, these nitrides have often been utilized as bulk or micrometer-sized powders, masking their novel functionalities. Recent research has highlighted the successful synthesis of a nitride-based anti-perovskite, Ni₃CuN nano-shell over Ni₃Cu core, emphasizing its potential as a catalyst for the CO₂ Reduction Reaction (RR).[17] The synthesis route, involving solvothermal synthesis of Ni₃Cu/C followed by calcination under NH₃, resulted in an anti-perovskite Ni₃CuN nano layer (Ni₃Cu@Ni₃CuN). Notably, upon introducing N into Ni₃Cu, more Lewis basic sites are created, leading to enhanced adsorption of CO₂ molecules and hydrogen reduction. Furthermore, the nanosizing effect resulted in higher oxidative state for the cation at the Ni site and deactivated the weaker Lewis basic site, thereby improving CO selectivity during the CO₂RR process. Thus, nano-sized anti-perovskite nitrides demonstrate high potential in controlling catalytic functions, underlining the importance of exploring further synthetic routes and material design to optimize catalyst functionality and performance.

The Polymer-derived ceramics (PDCs) route ensures strict control over the chemical composition, phase distribution, and the nano-/microstructure of final materials.[18] This bottom-up approach allows the growth of M and/or MN nanoparticles *in situ* distributed in a Si-based ceramic matrix.[19–31] The accessibility to metal nanoparticles/Si-based nanocomposites using the PDCs route and its advantages for catalytic applications have been discussed.[32] Recently, various M/Si-(oxy-)carbide (SiC, SiOC), Si-carb(oxy)nitride(SiCN, SiCON), and Si-nitride (Si₃N₄) matrix composites have been synthesized via the PDCs route, and some of these inorganic materials exhibit

[a.] Department of Life Science and Applied Chemistry, Graduate School of Engineering, Nagoya Institute of Technology, Gokiso-cho, Showa-ku, Nagoya 466-8555, Japan

[b.] University of Limoges, CNRS, IRCER, UMR 7315, F-87000, Limoges, France

[c.] Laboratory for High Performance Ceramics, Department of Metallurgical and Materials Engineering, Indian Institute of Technology Madras (IIT Madras), Chennai 600036, India

[d.] Department of Metallurgical and Materials Engineering, Indian Institute of Technology Madras (IIT Madras), Chennai 600036, India

excellent performance as robust and reusable heterogeneous catalysts in applications such as thermal catalytic hydrogenation and dehydrogenation of organic compounds,[21-25] the dehydrogenation of hydrides[30] and electrocatalytic water oxidation[26] under harsh conditions.

Our group previously reported the *in situ* formation of Co nanocrystallites embedded within amorphous silicon nitride (a-SiN) by thermal conversion under NH_3 atmosphere of a $CoCl_2$-coordinated perhydropolysilazane (PHPS) at a temperature as low as 400 °C.[33] Later on, we reported the detailed mechanistic study on the *in situ* formation of Ni/a-SiN compounds in flowing nitrogen. It proceeded via the easy thermal decomposition of Ni nitrides formed through the reaction of nickel chloride ($NiCl_2$) and PHPS as silicon nitride precursor at very low temperatures of 200 to 300 °C.[34] Finally, more recently, we investigated the catalytic activity of such materials.[35]

In the present work, we report the first example of isolating a nanoscale anti-perovskite nickel indium nitride (Ni_3InN) phase embedded within a-SiN (Fig. 1). This compound is generated by the low temperature pyrolysis of $NiCl_2$ and indium chloride ($InCl_3$)-*co*-modified polysilazanes (PSZs). The *in situ* formation mechanisms as well as the phase evolution upon pyrolysis are investigated based on a set of characterization techniques including elemental analyses, infrared spectroscopy, X-ray diffraction (XRD), thermogravimetric-mass spectrometry (TG-MS), X-ray photoelectron spectroscopy (XPS) and transmission electron microscopy (TEM). Finally, we reveal the unique carbon dioxide (CO_2) adsorption and desorption properties by measuring the temperature-programmed CO_2 desorption (CO_2-TPD) profile (Fig.1). This result offers additional functionalities aimed at activating and transforming small molecules into valuable products for clean energy applications.

Experimental section

Material synthesis

General procedure for the synthesis of anti-perovskite nitride/a-SiN nanocomposites. The chemicals and reagents were handled
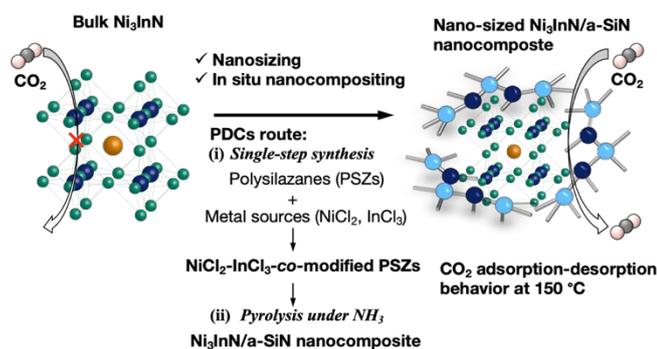
Fig. 1 Schematic illustration of the process to synthesize nano-sized anti-perovskite Ni_3InN/amorphous silicon nitride (a-SiN) nanocomposite through PDCs route, and the CO_2 adsorption-desorption behaviour for potential small molecule activation catalyst.

under an inert atmosphere of pure argon (Ar) using standard Schlenk techniques and vacuum/Ar lines. Commercially available poly(vinylmethyl-*co*-methyl) silazane (Durazane®1800, Sanwa Kagaku Co., Shizuoka, Japan), $NiCl_2$ (98 % purity, Merck Japan, Tokyo, Japan), $CoCl_2$ (97 % purity, Merck Japan, Tokyo, Japan), $InCl_3$ (98 % purity, Merck Japan, Tokyo, Japan) were used as received. Another PSZ, a commercially available perhydropolysilazane (PHPS, NN120-20, 20 wt% in dibutyl ether solution, Sanwa Kagaku Co., Shizuoka, Japan), was used (20 wt%) in super-anhydrous toluene (99.5 % purity, FUJIFILM Wako Pure Chemical Co., Osaka, Japan) after substitution of dibutyl ether. MCl_2 (M = Ni or Co) and $InCl_3$-co-modified PSZs were synthesized with different M/Si and In/Si atomic ratios (M/Si = 0.05 or 0.1, In/Si = 0.1). Herein, the synthesized precursors were labeled M_xIn_y-DRZ and M_xIn_y-PH (x and y represent the nominal M/Si and In/Si ratio, respectively) according to the type of the preformed polymers, *i.e.*, DRZ for Durazane®1800 and PH for PHPS, respectively. Here, we describe the synthesis of the representative $Ni_{0.1}In_{0.1}$-DRZ sample, which is prepared through a synthesis procedure applied for all precursors studied in this paper. A 100 mL two-neck round-bottom flask equipped with a magnetic stirrer was charged with Durazane®1800 (4 mL, 63 mmol) and toluene (40 mL), then $NiCl_2$ (0.84 g, 6.3 mmol, Ni/Si = 0.1), and $InCl_3$ (1.4 g, 6.3 mmol, In/Si = 0.1) were added to the solution at room temperature. The reaction mixture was vigorously stirred at room temperature for 30 min and subsequently refluxed at 110 °C for 15 h under flowing Ar. After the reaction mixture was cooled to room temperature, toluene was removed under vacuum at 60 °C to offer the $Ni_{0.1}In_{0.1}$-DRZ sample. After a complete characterization, as-synthesized precursors were pyrolyzed under flowing NH_3 at temperatures of 300, 400, and 600 °C for 2 h with a heating rate of 5 °C min^{-1}. The pyrolyzed samples were labeled M_xIn_y-DRZT, where T is the pyrolyzed temperature.

General procedure for the synthesis of bulk Ni_3InN. The bulk Ni_3InN sample was synthesized by following the reported procedure:[15] the stoichiometric amount of metal nitrates; Ni $(NO_3)_2·6H_2O$ (99.9 % purity, FUJIFILM Wako Pure Chemical Co., Osaka, Japan); and $In(NO_3)_3·3H_2O$ (97 %+ purity, FUJIFILM Wako Pure Chemical Co., Osaka, Japan) were dissolved in a minimal amount of 10 % HNO_3 aqueous solution and stirred at room temperature for 30 min. The resulting solution was dried overnight at 120 °C, followed by pyrolyzed in air at 400 °C for 3 h. Subsequently, the precursor oxide was heat-treated under flowing NH_3 at 600 °C for 10 h with a heating-cooling rate of 2.5 °C min^{-1}.

Characterization. As synthesized polymer samples were analyzed with Flourier transform infrared (FTIR) spectroscopy with an attenuated total reflection (ATR) attachment (Model ATR PRO 550S-S/570S-H, JASCO Corporation, Tokyo, Japan), performed on a FTIR spectrometer (Model FT/IR-4200IF, JASCO Corporation, Tokyo, Japan) with a resolution of 4 cm^{-1}. For the as-synthesized polymer samples, the TG-MS analysis up to 1000 °C under He was performed

by using TG-DTG equipment (Model STA7200, Hitachi High-Tech Science Corporation, Tokyo, Japan) coupled with a quadrupole mass-spectrometry (Model JMS-Q1500GC, JEOL Ltd., Tokyo, Japan) operating at a heating rate of 10 °C min⁻¹. Elemental analyses were performed for oxygen and nitrogen using the inert-gas fusion method (Model EMGA-930, HORIBA, Ltd., Kyoto, Japan) and for carbon using the non-dispersive infrared method (Model CS844, LECO Co., St Joseph, MI, USA). Energy dispersive X-ray spectrometry (EDS, Model JSM-6010LA, JEOL Ltd., Tokyo, Japan) was used to determine Si, Tm (Ni or Co), In, and Cl contents, and was performed on scanning electron microscope (SEM, Model JSM-6010LA, JEOL Ltd., Tokyo, Japan). Then, the chemical composition of pyrolyzed samples was calculated as reported previously.[33, 34] The powder XRD patterns were recorded for the pyrolyzed samples using Co$K\alpha$ radiation (Model Miniflex 600NB, Rigaku Co., ltd., Tokyo, Japan). The average crystallite size was calculated using the Scherrer equation. The microstructure observations were performed using a Schottky field emission SEM (FE-SEM, Model, JSM-7800F, JEOL Ltd., Tokyo, Japan) coupled with an energy-dispersive X-ray spectrometer (Model X-max, Oxford Instruments Holding 2013 Inc., Tokyo Japan) and a cathode luminescence detector (Model MonoCL4Elite, Gatan Inc., Pleasanton, CA, USA) and TEM. The TEM observations were performed on the selected samples using an atomic-resolution analytical microscope. **Ni$_{0.05}$In$_{0.1}$-DRZ600** sample was observed using JEM-ARM200F (JEOL Ltd., Tokyo, Japan), operating at an accelerating voltage of 200 kV. Textural properties of pyrolyzed samples were evaluated by measuring N$_2$ adsorption and desorption isotherms at −196 °C under relative pressures ranging from 0 to 0.99 (Model Belsorp Max, BEL Japan Inc., Osaka, Japan). The pore size distribution was analyzed by the micropore plot (MP)[36] and Barrett-Joyner-Halenda (BJH)[37] methods. X-ray photoelectron spectroscopic (XPS) measurements were performed using X-ray Photoelectron Spectrometer (PHI Quantes, ULVAC-PHI, Inc., Kanagawa, Japan) with an Al Ka (1486.6 eV) X-ray source. An alignment on the C 1s peak (284.8 eV) was performed on the survey and high-resolution spectra. To study the CO$_2$ adsorption and desorption properties, the temperature-programmed desorption of CO$_2$ (CO$_2$-TPD) profile was recorded using a catalyst analyzer (Model BELCAT-A, BEL Japan Inc., Osaka, Japan) equipped with a quadrupole mass spectrometer (Model BELMASS, BEL Japan Inc., Osaka, Japan). Prior to the measurement, the sample was maintained at 600 °C for 1 h under flowing He (50 mL min⁻¹). Subsequently, the sample was exposed to CO$_2$ at specific temperatures (50, 100, and 150 °C) for 30 min. The CO$_2$-TPD profiles were measured while heating from 50 to 500 °C (10 °C min⁻¹) under a flow of pure He (50 mL min⁻¹). The CO$_2$-TPD spectra were detected as a thermal conduction detector profile and a CO$_2$-mass (m/z = 44) profile.

Results and discussion

Synthesis and characterization of NiCl$_2$ and InCl$_3$-*co*-modified PSZs

We firstly synthesized NiCl$_2$-InCl$_3$-co-modified PSZs as precursors of the Ni$_3$InN/a-SiN nanocomposites. The chemical reaction between PSZs including Durazane®1800 (DRZ) and PHPS (PH) and metal chlorides was firstly monitored by FTIR (Fig. 2 and Fig. S1 in ESI). Regardless of the starting polymer,
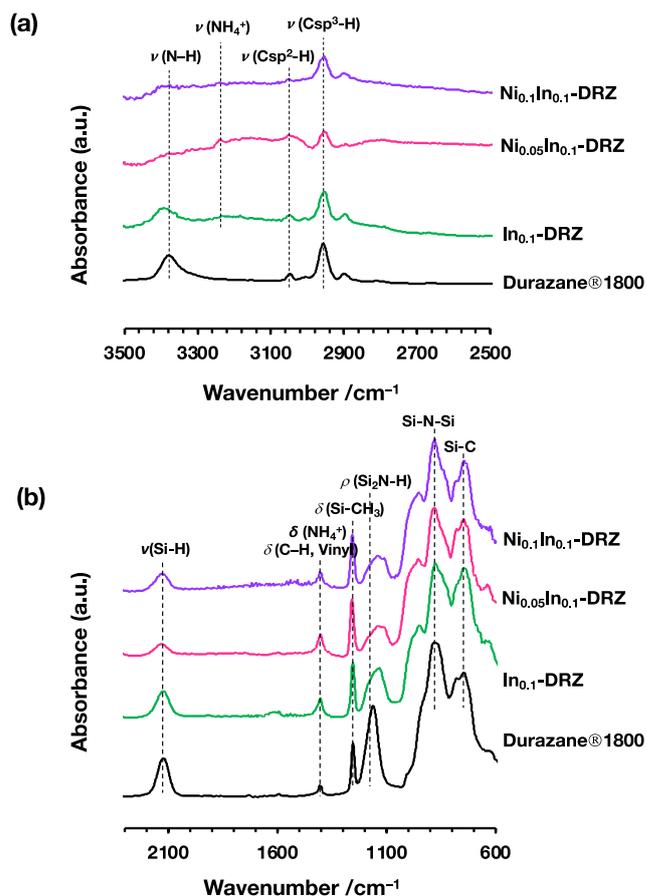
Fig. 2 ATR-FTIR spectra for starting Durazane®1800 and as-synthesized **Ni$_x$In$_{0.1}$-DRZ** samples (x = 0, 0.05 and 0.1) in the range of (a) 3500–2500 cm⁻¹ and (b) 2300–600 cm⁻¹.

the M/Si and In/Si molar ratios, the spectra for the CoCl$_2$-modified PSZs were quite similar to those for NiCl$_2$-modified PSZs. A representative ATR-FTIR spectroscopic analysis revealed spectral changes for the NiCl$_2$-InCl$_3$-*co*-modified DRZ based on different Ni/Si and In/Si molar ratios (Fig. 2). For comparison, the spectrum of the as-received Durazane®1800 was also recorded (Fig. 2 and Fig. S1 in ESI). FTIR band (ATR /cm⁻¹): 3379 (vN–H), 3048 (vC$_{sp2}$–H), 2957 (vC$_{sp3}$–H), 2121 (vSi–H), 1590 (vC=C), 1404 (δC–H, Vinyl), 1254 (δSi–CH$_3$), 1160 (ρSi$_2$N–H), 881 (vSi–N–Si), and 746 (vSi–C).[38–40] The changes in the position and the relative intensity to vSi–N–Si(I_{band}:$I_{Si-N-Si}$) of their selected absorption bands are listed in Table S1. As shown in Fig. 2b, the chemical modification of Durazane®1800 with NiCl$_2$ and InCl$_3$ resulted in a reduction in the relative intensity of the ρSi$_2$N–H and vSi–H bands. In our previous work, we proposed the mechanism behind these changes, enhancing the formation of ternary silylamino group via the NiCl$_2$ catalyzed dehydrocoupling reaction between N–H group and Si–H group present in PHPS and subsequently coordinated on Ni cation to afford Ni^{2+} complex (Scheme S1).[34] In the InCl$_3$-modified DRZ samples, the stretching vN–H vibration shifted to higher wavenumber (WN) values of approximately 3400 cm⁻¹ (Fig. 2a and Table S1), indicating a transformation of the ≡Si–NH–Si≡

bridging into terminal ≡Si–NH₂.[39] This alternation likely resulted from the partial cleavage of Si–N bonds through a transamination reaction during the refluxing process at 110 °C, as represented in Eq. 1a and Eq.1b.

$$2 \equiv Si–NH–Si\equiv \rightarrow \equiv Si–N(Si\equiv)–Si\equiv + \equiv Si–NH_2 \qquad \text{eq. (1a)}$$
$$\equiv Si–NH–Si\equiv + \equiv Si–NH_2 \rightarrow \equiv Si–N(Si\equiv)–Si\equiv + NH_3 \qquad \text{eq. (1b)}$$
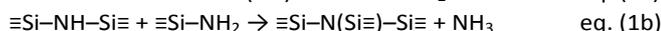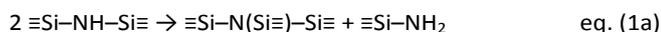
Subsequently, a new band emerged around 3240 cm⁻¹, while the relative intensity of a peak at 1404 cm⁻¹ slightly increased. These bands were assigned to ammonium ion (NH₄⁺).[41] These changes are possibly attributed to the combined effects of the transamination reaction (eq. (1)) and the acid-base reaction between ≡ Si–NH–Si ≡ and InCl₃ (eq. (2)), leading to the formation of ammonium chloride through the reaction between NH₃ (by product in eq. (1b)) and HCl (by-product in eq. (2)).

$$\equiv Si–NH–Si\equiv + InCl_3 \rightarrow \equiv Si–N(InCl_2)–Si\equiv + HCl \qquad \text{eq. (2)}$$

These reactions within the systems promote the self-crosslinking of the polysilazane, facilitating the molecular-scale integration of metal species through both coordination (with NiCl₂) and direct bond formation (with InCl₃). Similar trends are observed when PHPS is modified with NiCl₂ and InCl₃ (see Fig. S1 in ESI). Notably, the formation of NH₄⁺ is obvious in the FTIR spectrum when InCl₃ is introduced in the PHPS network. This result suggests that polymer structure and in particular the chemical environment around Si plays an important role in the occurrence of the reactions between PSZs and InCl₃. We suggest that the NiCl₂-InCl₃-*co*-modified PH is built via the acid-base reaction presented in Eq. 2 whereas using DRZ, this reaction is sterically hindered because of the presence of vinyl and methyl groups. It forms a weak π-coordinated InCl₃ complex (Scheme 1).

Polymer-to-ceramic conversion behaviour of NiCl₂-InCl₃-*co*-modified PSZs

To study the ceramic conversion behaviour of as-synthesized precursors, TG-MS analysis was conducted under He up to 1000 °C at a heating rate of 10 °C min⁻¹. Figures 3a and 3b show the
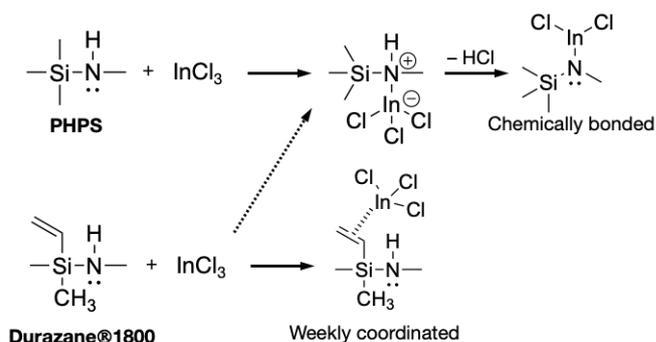
Scheme 1 The possible reactions of PSZs and InCl₃.

TG-curve for Durazane®1800 and as-synthesized samples (Fig. 3a), as well as the selected ion current chromatogram (Fig. 3b) simultaneously measured for the **Ni₀.₁In₀.₁-DRZ** sample. The TG-curve of as-received Durazane®1800 (Fig. 3a) indicates a weight loss segmented into three temperature ranges: 50– 300 °C (~13 wt%), 300–520 (~10 wt%), and 520–800 °C (~13 wt%). The final ceramic yield of Durazane®1800 pyrolyzed under He was 64.0 %, consistent with previously reported data.[36] The weight loss at 50-300 °C was notably suppressed in **Ni₀.₁In₀.₁-DRZ** and **Co₀.₁In₀.₁-DRZ** samples. However, the weight loss for the **In₀.₁-DRZ** sample in this temperature range is comparable to that of Durazane®1800. The known species responsible of the main weight loss of PSZs in this temperature range are low molecular weight organosilicon species and NH₃ caused by transamination reactions (see Fig. S2).[38] The lower weight loss recorded below 300°C for the **Ni₀.₁In₀.₁-DRZ** and **Co₀.₁In₀.₁-DRZ** samples could be due to their enhanced crosslinking, driven by reactions with MCl₂ (M = Ni and Co) during synthesis such as dehydrocoupling and transamination reactions (*see Eq. (1)*) in this system. Volatilization of chlorosilanes (*e.g.*, monochlorosilane; m/z = 78, 80, and dichlorosilane; m/z = 113, 115) starts at 200 °C (Fig. 3b). It is due to the *in situ* formation of Ni nitride species, originating from the Ni²⁺ complex, via the S_N2 reaction.[34] Therefore, MCl₂ is accessible to the ligand of PSZ for the in situ formation of Ni (Co) nitride intermediates and subsequent growth of Ni (Co) nanocrystallites during pyrolysis.
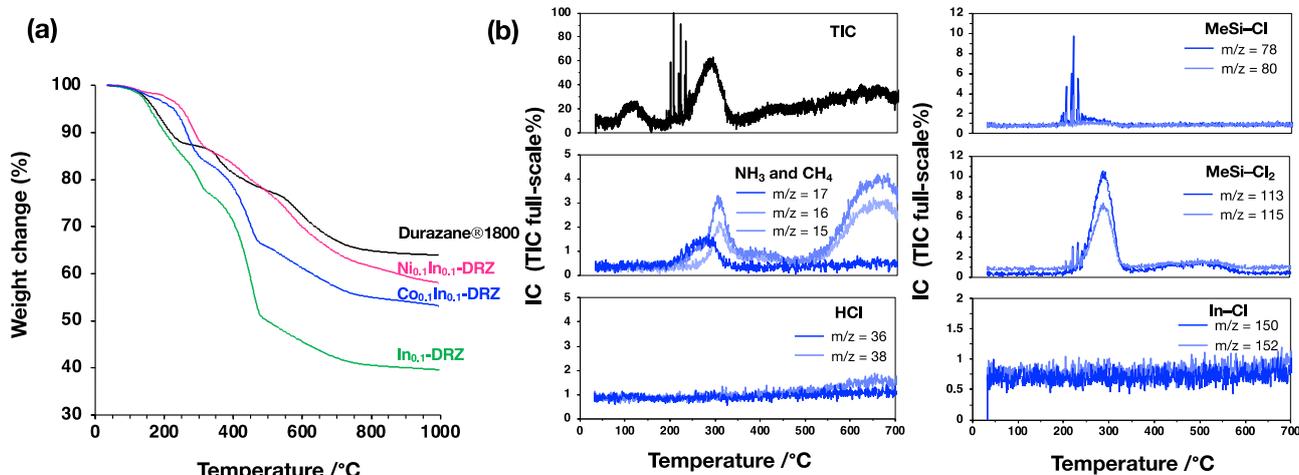
Fig. 3 (a) TG-curve of starting Durazane®1800 and as-synthesized **MₓIn₀.₁-DRZ** samples (M = Ni and Co, x = 0 or 0.1) to 1000 °C under He and (b) the total ion current (TIC) chromatogram and selected mass fragments measured for **Ni₀.₁In₀.₁-DRZ** sample during TG-MS analysis.
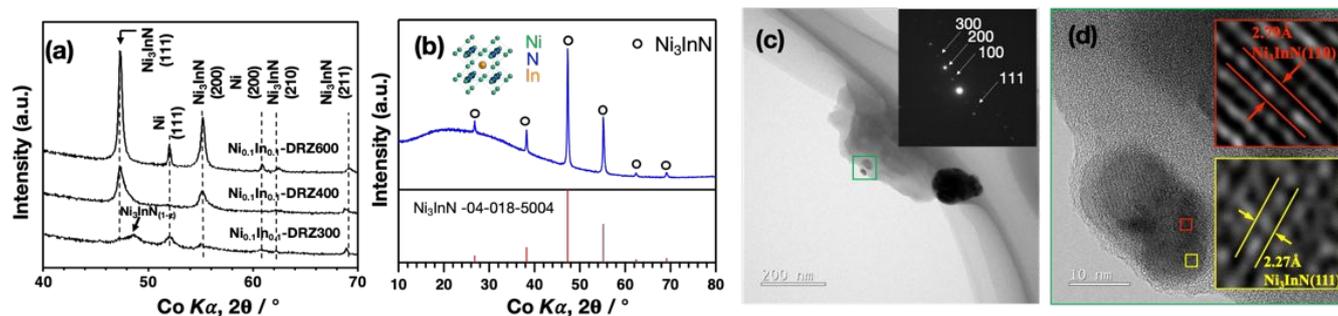
Fig. 4 Phase composition of Ni$_3$InN/a-SiN nanocomposites: XRD patterns of (a) **Ni$_{0.1}$In$_{0.1}$-DRZT** sample and (b) **Ni$_{0.05}$In$_{0.1}$-DRZ600** samples; (c) TEM image of **Ni$_{0.05}$In$_{0.1}$-DRZ600** sample, and the corresponding SAED pattern; and (d) HRTEM images of a selected area (green square in (c)), the insets in (d) show the lattice structure of the Ni$_3$InN nanocrystallites.

Volatilization of hydrochloric acid (HCl, m/z = 36 and 38) is not observed for the **Ni$_{0.1}$In$_{0.1}$-DRZ** sample (Fig. 3b), while a large amount of HCl was detected for the **Ni$_{0.1}$In$_{0.1}$-PH** sample (Fig. S3b). This confirms that the corresponding acid-base reaction between PSZs and InCl$_3$ (*Eq. (2)*) is limited for the **Ni$_{0.1}$In$_{0.1}$-DRZ** sample during the synthesis and pyrolysis. The weight loss from 300 °C to 500 °C is much more pronounced for the **In$_{0.1}$-DRZ** sample, likely due to the volatilization of InCl$_3$, which has been reported to occur at 330 °C in an inert atmosphere.[42] In contrast, the **In$_{0.1}$-PH** sample (Fig. S3a) displays a consistent gradient in this temperature range. Again, this is in good agreement with the occurrence of an acid-base reaction forming In-N bonds during synthesis decreasing the amount of unreacted InCl$_3$ which is known to evaporate at around 330 °C. XRD patterns presented in Fig. S4 for **In$_{0.1}$-DRZ** and **In$_{0.1}$-PH** samples, which have been pyrolyzed at 600 °C under NH$_3$ (namely, **In$_{0.1}$-DRZ600** and **In$_{0.1}$-PH600**) reveal these distinct differences. The XRD pattern of the **In$_{0.1}$-DRZ600** sample corresponds to that one of a X-ray amorphous material, whereas the XRD pattern of the **In$_{0.1}$-PH600** sample shows peaks corresponding to In species, specifically InCl (PDF #04-018-9284) and In (PDF #00-005-0642) that could indicate a partial reaction of InCl$_3$ with PHPS.

Compared to the **In$_{0.1}$-DRZ** sample, the lower weight loss of the **Ni$_{0.1}$In$_{0.1}$-DRZ** and **Co$_{0.1}$In$_{0.1}$-DRZ** samples indicated that volatilization of InCl$_3$ between 330–500 °C is much more limited (Fig. 3a). In particular, **Ni$_{0.1}$In$_{0.1}$-DRZ** sample exhibited a lower weight loss (10 wt%) which is even significantly less than the expected weight of InCl$_3$ incorporated in the **Ni$_{0.1}$In$_{0.1}$-DRZ** precursor (approximately 22 wt%). We therefore suggest that

the In species are trapped within the system facilitating the in situ formation of bimetallic alloy in conjunction with Ni species. Thus, TG-MS analysis highlights that the migration of In species into parental metals, which occurs *in situ* during pyrolysis, is pivotal for the formation of anti-perovskite nitride within the PSZ-derived a-SiN matrix.

In situ formation of anti-perovskite Ni$_3$InN in a-SiN

Pyrolysis under NH$_3$ leads to samples with tuned phase composition and nano-/microstructure organization according to the pyrolysis temperature (*T* = 300, 400, and 600 °C). Herein, the pyrolysis of the reference **Ni$_{0.1}$In$_{0.1}$-DRZ** has been monitored through the XRD analysis of the derived compounds isolated after heat treatment at 300 (**Ni$_{0.1}$In$_{0.1}$-DRZ300**), 400 (**Ni$_{0.1}$In$_{0.1}$-DRZ400**) and 600 (**Ni$_{0.1}$In$_{0.1}$-DRZ600**) °C (Fig. 4a). The XRD pattern of **Ni$_{0.1}$In$_{0.1}$DRZ300** sample exhibits broad peaks assigned to face-centered cubic (fcc) Ni (PDF #00-004-0850), and Ni$_3$InN (PDF #04-018-5004). Remarkably, the *in situ* growth of fcc-Ni and anti-perovskite Ni$_3$InN initiates at temperatures as low as 300 °C. A transitional phase, nitrogen-deficient Ni$_3$InN$_{1-z}$ is also detected around 49°.[15] As the pyrolysis temperature elevates, the peak intensity for Ni$_3$InN increases, while the shoulder peak of Ni$_3$InN$_{1-z}$ disappears. In contrast, the peak intensity of *in situ* formed fcc Ni diminishes in **Ni$_{0.1}$In$_{0.1}$-DRZ400** and remains as a minor phase in **Ni$_{0.1}$In$_{0.1}$-DRZ600**, suggesting the transformation of Ni nanocrystallites into cubic Ni$_3$InN nanocrystallites. As shown in Fig. S5a, a similar trend is obtained for the XRD patterns of **Ni$_{0.1}$In$_{0.1}$-PHT** (T = 300, 400, 600) samples. To further understand the thermal behavior of **Ni$_x$In$_y$-DRZ** sample, we have studied the XRD pattern of the **Ni$_{0.05}$In$_{0.1}$-**

Table 1 Chemical compositions of as-pyrolyzed **Ni$_x$In$_{0.1}$DRZT** samples (x = 0.05 and 0.1, T = 300, 400, and 600).

	Composition (wt%)							
Name	Si	C	N	O	Ni	In	Cl	Atomic ratio normalized on Si
Ni$_{0.05}$In$_{0.1}$-DRZ600	44.69	0.33	35.67	5.55	3.02	2.40	8.35	Si$_1$C$_{0.02}$N$_{1.60}$O$_{0.22}$Ni$_{0.03}$In$_{0.01}$Cl$_{0.15}$
Ni$_{0.1}$In$_{0.1}$-DRZ300	40.49	4.47	16.57	1.73	12.15	14.73	9.86	Si$_1$C$_{0.26}$N$_{0.82}$O$_{0.07}$Ni$_{0.14}$In$_{0.09}$Cl$_{0.19}$
Ni$_{0.1}$In$_{0.1}$-DRZ400	45.35	0.59	19.48	1.86	8.88	14.40	9.44	Si$_1$C$_{0.03}$N$_{0.86}$O$_{0.07}$Ni$_{0.09}$In$_{0.08}$Cl$_{0.17}$
Ni$_{0.1}$In$_{0.1}$-DRZ600	50.15	0.29	26.62	4.02	9.91	5.45	3.57	Si$_1$C$_{0.01}$N$_{1.06}$O$_{0.14}$Ni$_{0.09}$In$_{0.03}$Cl$_{0.06}$

DRZ600 sample (Fig. 4b); thus, with a lower Ni content. Interestingly, it shows a single cubic phase (space group: *Pm-3m*) corresponding to anti-perovskite Ni_3InN. A highly diffuse peak in the 2θ range of 10–50 ° suggests the presence of an amorphous phase; most probably related to the presence of the a-SiN matrix. According to Scherrer's formula, the average crystalline size of Ni_3InN (111) plane for the **Ni$_{0.05}$In$_{0.1}$-DRZ600**, was calculated to be 32.8 nm.

The chemical compositions of as-pyrolyzed **Ni$_{0.1}$In$_{0.1}$-DRZT** and **Ni$_{0.05}$In$_{0.1}$-DRZ600** samples are summarized in Table 1, while the chemical compositions of **Ni$_{0.1}$In$_{0.1}$-PHT** samples are listed in Table S2. During the pyrolysis under NH_3 from 300 to 600 °C, the In/Si ratio of **Ni$_{0.1}$In$_{0.1}$-DRZT** samples consistently decreased as the pyrolysis temperature increased. This trend is attributed to the evolution of In species as detailed in the TG-MS analysis. In contrast, the **Ni$_{0.1}$In$_{0.1}$-PHT** samples maintained the In/Si ratio constant even at temperatures above 400 °C (**Ni$_{0.1}$In$_{0.1}$-PH400** and **Ni$_{0.1}$In$_{0.1}$-PH600**). For the **Ni$_{0.05}$In$_{0.1}$-DRZ600** and **Ni$_{0.1}$In$_{0.1}$-DRZ600** samples, the measured Ni/In atomic ratios were calculated to be 3, aligning with the Ni/In atomic ratio expected for the Ni_3InN. Therefore, an excess of In species is found to be required at the precursor level to afford the anti-perovskite Ni_3InN phase while the formation of secondary metal-based phases is hindered in the a-SiN matrix as successfully achieved for the **Ni$_{0.05}$In$_{0.1}$-DRZ600** sample (the nominal Ni/In ratio of 0.5).

Interestingly, under the given synthesis condition, the anti-perovskite Co_3InN phase[43] does not form by replacing $NiCl_2$ by $CoCl_2$ to react with Durazane®1800 Figure S5b shows the evolution of the XRD patterns of **Co$_{0.1}$In$_{0.1}$-DRZ*T*** samples from 300 to 600 °C. The **Co$_{0.1}$In$_{0.1}$-DRZ300** sample exhibits characteristic peaks at 48.7, 52.0, and 55.6 ° assigned to hexagonal-close-packed (hcp) Co (PDF #01-089-4308). The **Co$_{0.1}$In$_{0.1}$-DRZ400** and **Co$_{0.1}$In$_{0.1}$-DRZ600** samples exhibit the diffraction peaks at 51.8 and 60.4 ° assigned to fcc Co (PDF #00-015-0806); 48.5, 51.8, and 55.6 ° assigned to hcp Co, respectively. The chemical composition of **Co$_{0.1}$In$_{0.1}$-DRZ*T*** samples is summarized in Table S3. The In/Si atomic ratio of **Co$_{0.1}$In$_{0.1}$-DRZ*T*** samples consistently decreased with increasing the pyrolysis temperature, and the final Co/In atomic ratio is calculated to be 11 in the **Co$_{0.1}$In$_{0.1}$-DRZ600** samples. As highlighted in the TG-MS analysis (Fig. 3a), a significant difference in weight loss between **Ni$_{0.1}$In$_{0.1}$-DRZ** and **Co$_{0.1}$In$_{0.1}$-DRZ** is observed at 300–500 °C range, with values of 10% for **Ni$_{0.1}$In$_{0.1}$-DRZ**, and 19 % for **Co$_{0.1}$In$_{0.1}$-DRZ**. This suggests that the volatilization of $InCl_3$ between 330–500 °C may influence the *in situ* formation of intermetallic compounds. The hcp Co and fcc Ni phases remain dominant at 300 °C, where the evaporation of In species takes place. A deep examination of the XRD patterns of the **Co$_{0.1}$In$_{0.1}$-DRZ300** sample (Fig. S5b) reveals the existence of additional peaks on the higher angle side for the (100) plane of hcp Co and on the lower angle side for the (002) and (101) planes. These shifts towards higher and lower angles, respectively, suggest alterations of the crystalline lattice, possibly due to the insertion of In species. Importantly, with the Co particles aligned parallel to the (002) and (101) planes, it is likely that the insertion of In species takes place
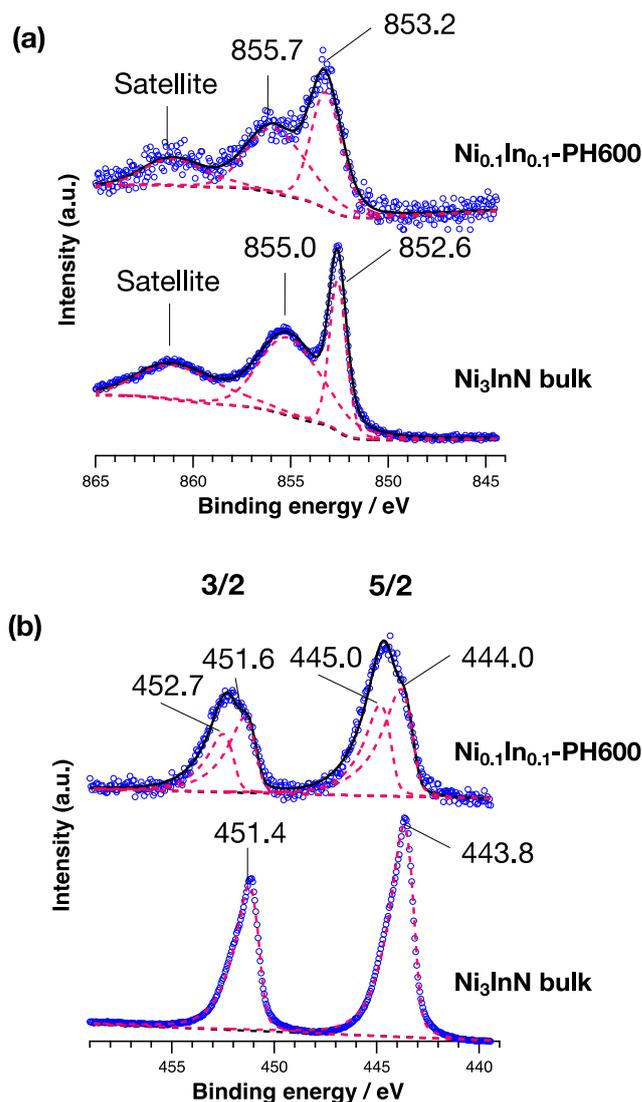
Fig. 5 XPS spectra of (a) Ni $2p_{3/2}$ and (b) In $3d$ for the Ni_3InN/a-SiN nanocomposite (**Ni$_{0.1}$In$_{0.1}$-PH600**) and bulk Ni_3InN samples.

along these planes, leading to lattice expansion perpendicular to them.

On the other hand, the fcc phase of Ni is the predominant phase at 300 °C, which suggests a more straightforward insertion and migration process for In species within Ni. This allows the In atoms to position themselves favorably for Ni_3InN nucleation. Thus, Ni (with its fcc structure) presents more suitable phase compatibility for Ni_3InN nucleation compared to Co (with its hcp structure) for Co_3InN nucleation. This difference likely limits the subsequent transformation into the anti-perovskite nitride in the **Co$_{0.1}$In$_{0.1}$-DRZ600** samples. These results suggest that the formation mechanism of anti-perovskite Ni_3InN nanoparticles involves crucial steps of processes within the NiIn-DRZ system: Initially, Ni nanoparticles are formed in situ at temperatures below 300 °C. Subsequently, the migration of In species into these nanoparticles triggers a transformation process. This migration occurs notably below 400 °C due to the weak coordination nature of the In species, as depicted in Scheme 1,

and this migration of In into Ni nanoparticles is considered pivotal for the in situ formation of Ni_3InN. On the other hand, a precise understanding of the nitridation process remains a continuous subject, however, we found that pyrolysis under an ammonia atmosphere is crucial for the Ni_3InN formation through the PDCs route investigated in this study.

For a detailed insight into the micro- and nano-structures, TEM investigations have been performed on the **$Ni_{0.05}In_{0.1}$-DRZ600** sample. The TEM images (Fig. 4c and Fig. S6a) exhibit the darker contrast of nanocrystallites embedded within an amorphous matrix. The selected area electron diffraction (SAED) pattern shown in the inset of Fig. 4c is composed of well-defined spots, indicating the high crystallinity of the analyzed phase, and confirming the identification of an anti-perovskite Ni_3InN phase. The nanoparticle size ranges from 20 to 80 nm with a broad size distribution, as shown in Fig. S6c. The high-resolution (HR) TEM image (Fig. 4d), focusing on the selected area marked by the green square in Fig. 4c, reveals an embedded Ni_3InN nanophase within an amorphous matrix. Nanoparticles display lattice spacings of 2.27 and 2.79 Å, corresponding to the d-spacing of (111) and (110) planes of the Ni_3InN phase, respectively. Furthermore, the HAADF-STEM image (Fig. S6b) and corresponding STEM-energy-dispersive X-ray spectroscopy (EDS) mapping analysis (Fig. S6d–f) show excellent consistency between the elemental distributions of Ni and In within the a-SiN matrix, which confirms the growth of the Ni_3InN nanophase. SEM-EDS mapping analysis for the Ni_3InN/a-SiN nanocomposite is presented in Fig. S7 (using **$Ni_{0.1}In_{0.1}$-PH600** sample). Similar to the STEM-EDS mapping analysis, the distributions of Ni and In species (Figs. S7d and S7e) are consistent with each other, confirming the in situ formation of single-phase Ni_3InN nanoparticles. A pronounced darker N contrast in a more monolithic configuration highlights the nitrogen-deficient nature of the surrounding amorphous matrix (as depicted in Fig. S7c). This suggests that the nitrogen atoms of PSZ are involved in the formation of Ni_3InN nanoparticles. Supporting this observation, the SEM-CL image (Fig. S7h) captures emission from this nitrogen-deficient region, implying the presence of nitrogen-vacancy sites in this area.

The chemical bonding state of Ni_3InN/a-SiN nanocomposites was characterized by measuring XPS as shown in Fig. 5. For this characterization, **$Ni_{0.1}In_{0.1}$-PH600** sample has been selected, which is confirmed to predominantly consists of the Ni_3InN phase (as shown in Fig. S5b). The bulk Ni_3InN sample is also synthesized as a reference through the nitridation of the oxide precursor.[15] The survey scans of the Ni_3InN/a-SiN (**$Ni_{0.1}In_{0.1}$-PH600** sample) and the bulk Ni_3InN shown in Fig. S8 confirm the presence of all constituent elements. For the Ni $2p_{3/2}$ region of Ni_3InN/a-SiN nanocomposites (Fig 5a), the deconvolution of Ni $2p_{3/2}$ at 853.2 and 855.7 eV represents Ni^0 and Ni^{2+}, respectively.[44] The binding energy of Ni $2p_{3/2}$ peaks slightly shift to higher binding energies than those of bulk Ni_3InN, suggesting the presence of positively charged $Ni^{\delta+}$ species. The In $3d_{5/2}$ and $3d_{3/2}$ regions of Ni_3InN/a-SiN nanocomposite have been fitted with two peaks; the deconvolution of In $3d_{5/2}$ peak yields two peaks at 444.0 and 445.0 eV, and the deconvolution of In $3d_{3/2}$ peak yields two peaks at 451.6 and 452.7 eV, respectively. The

sub-peaks presented at higher binding energy than In^0 (445.0 eV for In $3d_{5/2}$, 452.7 eV for $3d_{3/2}$) are assigned to $In^{\delta+}$, which may belong to In–N or In–O within the a-SiN matrix.[45] Because the precursors include metal chlorides, the influence of residual chlorine atoms (Table S2, approximately 3.67 wt %) on the shift in the XPS spectra should be considered. The EDS mapping analysis of the as-pyrolyzed sample (Fig. S7f) has shown that the chlorine atoms are mainly distributed in the a-SiN matrix and more outer areas rather than close to the nanocrystalline islands. This distribution is due to the free chlorine atoms reacting with the Si center of PSZ during the in situ formation of metal nanocrystallites as discussed in the previous study.[33,34] Furthermore, according to the NIST X-ray Photoelectron Spectroscopy Database,[46] Ni–Cl and In–Cl peaks are detected at ~1 eV higher binding energy compared to typical nickel and indium oxide. We could not identify such subpeaks in our XPS data. Therefore, the presence of a surrounding a-SiN matrix increases the interfacial area of Ni_3InN and a-SiN, suggesting that this affects the oxidation state of the anti-perovskite Ni_3InN. We suggest that $Ni^{\delta+}$ and $In^{\delta+}$ are formed primarily due to electron transfer from Ni^0, Ni^{2+}, and In^0 to the a-SiN matrix. As possible interactions, the Ni and In atoms could interact with N or defect sites (*i.e.*, N vacancy detected in SEM-EDS-CL images) of a-SiN matrix in addition to the interstitial N of Ni_3InN.

CO_2 adsorption-desorption behaviour of Ni_3InN/a-SiN nanocomposite

As a proof of concept, we have investigated the CO_2 adsorption-desorption behaviour of the title compounds.

To assess the gas accessibility to catalytically active sites of Ni_3InN/a-SiN nanocomposite materials, we have first characterized the textural properties of the compounds. Figure. S9 shows the N_2 adsorption and desorption isotherms at −196 °C and the pore size distributions for the **$Ni_{0.05}In_{0.1}$-DRZ600** sample. The sample exhibits types I and IV isotherms according to the IUPAC classifications[47,48] with the most distinct uptake at $p/p_0 < 0.1$ associated with the filling of micropores. The hysteresis loop identified at $p/p_0 > 0.5$ can be classified as H4 loop, generally found with mesoporous zeolite and micro-mesoporous carbons.[48] The pore size distribution curve is characterized by micropore plot (MP)[36] and Barrett-Joyner-Halenda (BJH)[37] method, showing that dominant peaks at 0.7 nm in the microporous (0.7–2nm) range (Fig. S9b) and 4.2 nm in the mesoporous (2–10 nm) range (Fig. S9c), respectively. In contrast, the N_2 adsorption and desorption isotherms of the **$Ni_{0.1}In_{0.1}$-PH600** sample (Fig. S10a) exhibit type III isotherm with a slight hysteresis loop, indicating that the **$Ni_{0.1}In_{0.1}$-PH600** sample is non-porous. The N_2 adsorption and desorption isotherms of the **$Ni_{0.1}In_{0.1}$-DRZ600** sample (Fig. S11a) show type I isotherms with a slight hysteresis loop, indicating the formation of micro-/meso-porous compounds. The Brunauer–Emmett–Teller (BET) surface areas and pore volumes are summarized in Table S4. The resulting BET surface area (SSA) of the **$Ni_{0.1}In_{0.1}$-PH600**, **$Ni_{0.1}In_{0.1}$-DRZ600** and **$Ni_{0.05}In_{0.1}$-DRZ600** samples are measured to be 32, 315, and 460 m^2 g^{-1}, respectively. The total pore volume ($V_{BET, total}$) of **$Ni_{0.1}In_{0.1}$-**

ARTICLE   **Journal Name**

PH600, **Ni$_{0.1}$In$_{0.1}$-DRZ600** and **Ni$_{0.05}$In$_{0.1}$-DRZ600** samples were measured to be 0.18, 0.19 and 0.38 cm^3 g^{-1}, respectively. The formation of micro-/meso-pore is significantly affected by both the pyrolysis environment and the chemical composition of preceramic polymer.[49] In this study, the differences in polymer composition between Durazane®1800—which contains vinyl and methyl groups— and carbon-free PHPS had a significant contribution to the initial porosity. Specifically, the micropore formation from DRZ is mainly due to the volatilization of gas components, such as hydrocarbons, during pyrolysis at temperatures exceeding 350 °C under NH$_3$. This phenomenon has been thoroughly discussed in PDCs.[49,50] Also, we suggest that InCl$_3$ species contribute to the pore formation during pyrolysis: the degree of mesopore formation depends on the relative amount of InCl$_3$ to Ni as shown in **Ni$_x$In$_{0.1}$-DRZ600** (x = 0.05 or 0.1) samples (see Fig. S9c and Fig. S11c). The excess of In species coordinated with PSZs are volatilized during the pyrolysis under NH$_3$ which means that InCl$_3$ plays the role of a template for developing the micro-/meso-porosity formation. Accordingly, the N$_2$ adsorption-desorption isotherm, and the pore size distributions of **In$_{0.1}$-DRZ600** sample (Fig. S12)—which is synthesized by the ammonolysis of **In$_{0.1}$-DRZ** sample at 600 °C— highlights the formation of a microporous matrix.

The formation of a high SSA a-SiN matrix surrounding nanometer-sized metal nanoparticles supposes that the latter are accessible.[25,33] Therefore, it has been expected to serve as catalytic active sites. Thus, we have probed the adsorption and CO$_2$ desorption properties using CO$_2$-TPD measurements as an illustrative case. Figures 6a–c show CO$_2$-TPD spectra recorded under He after CO$_2$ treatment at specific temperatures (T_{CO2} = 50 °C, 100 °C and 150 °C). In this study, the highest SSA sample has been compared with the microporous sample derived from In-modified Durazane®1800 (**In$_{0.1}$-DRZ600**)— and the bulk Ni$_3$InN sample. As depicted in Fig. 6a, following CO$_2$ treatment at T_{CO2} = 50 °C, the CO$_2$-TPD spectrum of micro-/mesoporous **Ni$_{0.05}$In$_{0.1}$-DRZ600** sample displays a broad signal ranging from approximately 50 to 350 °C. In contrast, the CO$_2$-TPD spectra of
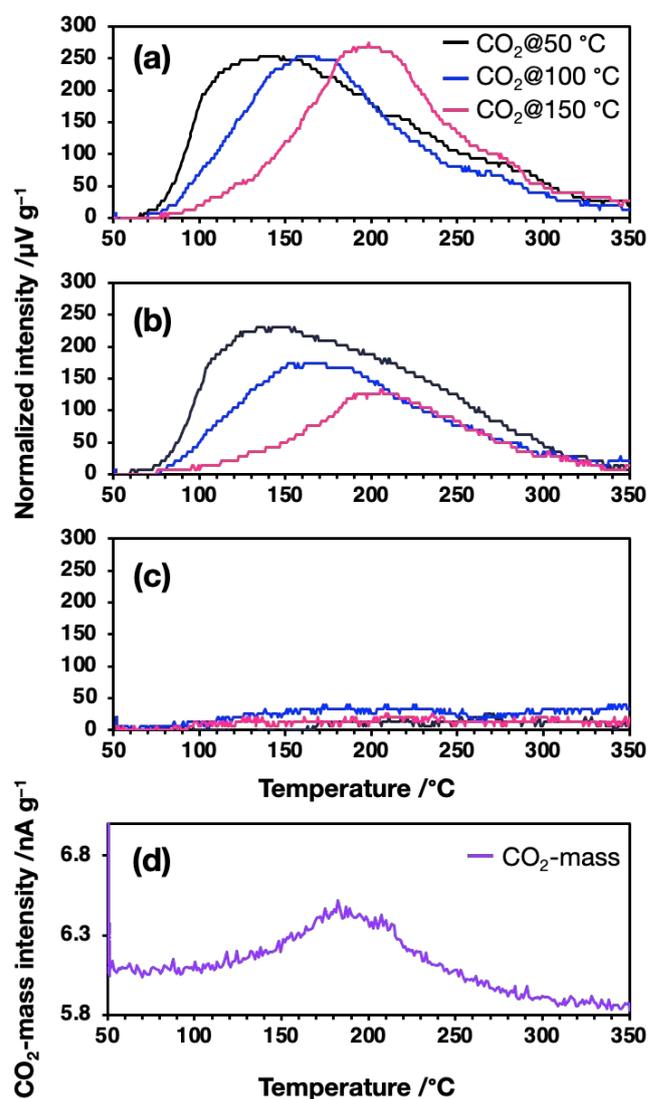
Fig. 6 CO$_2$-TPD spectra under flowing He recorded for Ni$_3$InN/a-SiN nanocomposites: Normalized TCD curves of (a) **Ni$_{0.05}$In$_{0.1}$-DRZ600** sample, (b) bulk Ni$_3$InN obtained by ammonolysis of oxide precursor and (c) microporous amorphous SiN derived from **In$_{0.1}$-DRZ600** synthesized by pyrolysis under NH$_3$ at 600 °C and (d) CO$_2$-mass spectra of **Ni$_{0.05}$In$_{0.1}$-DRZ600** sample recorded after CO$_2$ treatment at 150 °C.

the bulk Ni_3InN sample (Fig. 6b) exhibit no pronounced peak under the same measurement conditions. Interestingly, the CO_2 desorption peak intensity of the **$Ni_{0.05}In_{0.1}$-DRZ600** sample increases consistently with increasing T_{CO2}, suggesting the CO_2 chemisorption behavior (Fig. 6c). In contrast, the **$In_{0.1}$-DRZ600** sample exhibits a broad CO_2 desorption curve which decreases in intensity with increasing T_{CO2}, indicating CO_2 physisorption behavior. The simultaneous *in situ* mass analysis for **$Ni_{0.05}In_{0.1}$-DRZ600** sample (Fig. 6d) confirms the desorption of CO_2 (m/z = 44) at T_{CO2} = 150 °C. The results of XPS analysis shown in Fig. 5 indicate that the electronic structure of Ni_3InN in the nanocomposite system is remarkably more polar than the bulk Ni_3InN. This polarization is attributed to the presence of $Ni^{\delta+}$ and $In^{\delta+}$. The CO_2 chemisorption process could be facilitated with the polar sites through dipole interaction. Furthermore, the SEM-CL image (Fig. S7g) suggests the introduction of nitrogen defects into the a-SiN matrix that surrounds the Ni_3InN nanoparticles. These nitrogen defects potentially contribute to the adsorption of CO_2. The specific mechanism behind this phenomenon remains unclear at present. Nonetheless, these observations are expected to offer additional functionalities for the activation and transformation of such small molecules into valuable products as a novel energy-related catalyst, although clarifying the dominant mechanism requires further investigation.

Conclusions

In this study, we introduced a straightforward, one-step, low-temperature synthesis of anti-perovskite nitride nanoparticles via an *in situ* growth method labeled PDCs. We particularly examined the *in situ* formation of a nanoscale anti-perovskite Ni_3InN phase in an a-SiN matrix from a $NiCl_2$-$InCl_3$-*co*-modified PSZ. We also demonstrated the unique CO_2 adsorption and desorption property of the title compounds for their potential application as a novel energy-related catalyst.

(i) XRD and HRTEM observation revealed the *in situ* formation of anti-perovskite Ni_3InN within an amorphous SiN matrix started at a temperature as low as 300 °C.

(ii) FTIR and TG-MS analysis revealed that the *in situ* formation of parental metal Ni at a low temperature as low as 300 °C followed by the migration of the In species governed the in situ formation of anti-perovskite Ni_3InN. Moreover, it was found that the degree of cross-linking of the polysilazane network, and the distribution of In species were governed by the polymer architecture, chemical environment around major elements (*i.e.*, the steric hindrance) and chemical reactions that occurred during synthesis.

(iii) The XPS measurement suggested that the chemical bonding nature of the anti-perovskite Ni_3InN in the a-SiN changes the electronic structure of the metallic species (Ni or In): Ni and In consist of the mixed valence state of metallic (Ni^0 and In^0) and positively charged ($Ni^{\delta+}$ and $In^{\delta+}$) state as a result of *in situ* immobilization within the a-SiN matrix.

(iv) The unique CO_2 chemisorption behaviour of Ni_3InN/a-SiN was successfully demonstrated which is expected to offer additional functionalities for activating and transforming small molecules into valuable products for clean energy applications.

Author Contributions

S. Tada is responsible for the conceptualization, data curation, formal analysis, and writing the original manuscript of this work; S. Takazawa and N. Asakuma contributed to the evaluation of samples; S. Honda contributed to the formal analysis; R. Kumar N V reviewed the draft; S. Bernard reviewed the draft; Y. Iwamoto is responsible for the conceptualization, review and editing, and supervision of the manuscript.

Conflicts of interest

There are no conflicts to declare

Notes and references

1 Z. Lin, S. R. Denny and J. G. Chen, Transition metal carbides and nitrides as catalysts for thermochemical reactions, *J. Catal.*, 2021, **404**, 929–942.

2 Z. Cheng, W. Qi, C. H. Pang, T. Thomas, T. Wu, S. Liu and M. Yang, Recent Advances in Transition Metal Nitride-Based Materials for Photocatalytic Applications, *Adv. Funct. Mater.*, 2021, **31**, 2100553.

3 H. Wang, J. Li, K. Li, Y. Lin, J. Chen, L. Gao, V. Nicolosi, X. Xiao and J. M. Lee, Transition metal nitrides for electrochemical energy applications, *Chem. Soc. Rev.*, 2021, **50**, 1354–1390.

4 M.-H. Yu, L. H. Lewis and A. R. Moodenbaugh, Large magnetic entropy change in the metallic antiperovskite Mn_3GaC, *J. Appl. Phys.*, 2003, **93**, 10128–10130.

5 T. Tohei, H. Wada and T. Kanomata, Negative magnetocaloric effect at the antiferromagnetic to ferromagnetic transition of Mn_3GaC, *J. Appl. Phys.*, 2003, **94**, 1800–1802.

6 B. S. Wang, P. Tong, Y. P. Sun, X. Luo, X. B. Zhu, G. Li, X. D. Zhu, S. B. Zhang, Z. R. Yang, W. H. Song and J. M. Dai, Large magnetic entropy change near room temperature in antiperovskite $SnCMn_3$, *Europhysics Lett.*, 2009, **85**, 47004.

7 K. Takenaka, K. Asano, M. Misawa and H. Takagi, Negative thermal expansion in Ge-free antiperovskite manganese nitrides: Tin-doping effect, *Appl. Phys. Lett.*, 2008, **92**, 011927.

8 K. Takenaka and H. Takagi, Zero thermal expansion in a pure-form antiperovskite manganese nitride, *Appl. Phys. Lett.*, 2009, **94**, 131904.

9 Y. Zhao and L. L. Daemen, Superionic Conductivity in Lithium-Rich Anti-Perovskites, *J. Am. Chem. Soc.*, 2012, **134**, 15042–15047.

10 J. A. Dawson, T. Famprikis and K. E. Johnston, Anti-perovskites for solid-state batteries: recent developments, current challenges and future prospects, *J. Mater. Chem. A*, 2021, **9**, 18746–18772.

11 T. He, K. A. Regan, N. Rogado, M. A. Hayward, M. K. Haas, J. S. Slusky, K. Inumara, H. W. Zandbergen and R. J. Cava, Superconductivity in the non-oxide perovskite $MgCNi_3$, *Nature*, 2001, **411**, 54–56.

12 J. H. Shim, S. K. Kwon and B. I. Min, Electronic structures of antiperovskite superconductors $MgXNi_3$ (X = B, C, and N), *Phys. Rev. B*, 2001, **64**, 180510.

13 M. Uehara, A. Uehara, K. Kozawa, T. Yamazaki and Y. Kimishima, New antiperovskite superconductor $ZnNNi_3$, and related compounds $CdNNi_3$ and $InNNi_3$, *Phys. C Supercond. its Appl.*, 2010, **470**, S688–S690.

14 Y. Wang, H. Zhang, J. Zhu, X. Lü, S. Li, R. Zou and Y. Zhao, Antiperovskites with Exceptional Functionalities, *Adv. Mater.*, 2020, **32**, 1–17.

15 Y. Goto, A. Daisley and J. S. J. Hargreaves, Towards anti-perovskite nitrides as potential nitrogen storage materials for chemical looping ammonia production: Reduction of Co_3ZnN, Ni_3ZnN, Co_3InN and Ni_3InN under hydrogen, *Catal. Today*, 2021, **364**, 196–201.

16 A. Daisley, M. Higham, C. R. A. Catlow and J. S. J. Hargreaves, Experimental and theoretical investigations on the anti-perovskite nitrides Co_3CuN, Ni_3CuN and Co_3MoN for ammonia synthesis, *Faraday Discuss.*, 2023, **243**, 97–125.

17 Q. Liang, Y. Zhao, J. De Chen, J. J. Dai, X. Ding, Z. Tong, S. J. Xie, J. Zhang, Z. H. Zhou, J. T. Li, J. F. Li and Y. Zhou, Interfacial Electron Delocalization in Engineering Nanosized Anti-Perovskite Nitride for Efficient CO_2 Electroreduction, *Chem. Mater.*, 2022, **34**, 5607–5620.

18 P. Colombo, G. Mera, R. Riedel and G. D. Sorarù, Polymer-derived ceramics: 40 Years of research and innovation in advanced ceramics, *J. Am. Ceram. Soc.*, 2010, **93**, 1805–1837.

19 M. Zaheer, T. Schmalz, G. Motz and R. Kempe, Polymer derived non-oxide ceramics modified with late transition metals, *Chem. Soc. Rev.*, 2012, **41**, 5102.

20 M. Seifollahi Bazarjani, H. J. Kleebe, M. M. Müller, C. Fasel, M. Baghaie Yazdi, A. Gurlo and R. Riedel, Nanoporous silicon oxycarbonitride ceramics derived from polysilazanes in situ modified with nickel nanoparticles, *Chem. Mater.*, 2011, **23**, 4112–4123.

21 G. Glatz, T. Schmalz, T. Kraus, F. Haarmann, G. Motz and R. Kempe, Copper-containing SiCN precursor ceramics (Cu@SiCN) as selective hydrocarbon oxidation catalysts using air as an oxidant, *Chem. - A Eur. J.*, 2010, **16**, 4231–4238.

22 M. Zaheer, J. Hermannsdörfer, W. P. Kretschmer, G. Motz and R. Kempe, Robust heterogeneous nickel catalysts with tailored porosity for the selective hydrogenolysis of aryl ethers, *ChemCatChem*, 2014, **6**, 91–95.

23 S. M. Sachau, M. Zaheer, A. Lale, M. Friedrich, C. E. Denner, U. B. Demirci, S. Bernard, G. Motz and R. Kempe, Micro-/Mesoporous Platinum-SiCN Nanocomposite Catalysts (Pt@SiCN): From Design to Catalytic Applications, *Chem. - A Eur. J.*, 2016, **22**, 15508–15512.

24 D. Forberg, T. Schwob, M. Zaheer, M. Friedrich, N. Miyajima and R. Kempe, Single-catalyst high-weight% hydrogen storage in an N-heterocycle synthesized from lignin hydrogenolysis products and ammonia, *Nat. Commun.*, 2016, **7**, 1–6.

25 D. Forberg, T. Schwob and R. Kempe, Catalytic condensation for the formation of polycyclic heteroaromatic compounds, *Nat. Commun.*, 2018, **9**, 1751.

26 R. K. Morais Ferreira, M. Ben Miled, R. K. Nishihora, N. Christophe, P. Carles, G. Motz, A. Bouzid, R. Machado, O. Masson, Y. Iwamoto, S. Célérier, A. Habrioux and S. Bernard, Low temperature in situ immobilization of nanoscale fcc and hcp polymorphic nickel particles in polymer-derived Si-C-O-

27 Y. Iwamoto, K. Kikuta and S. Hirano, Si_3N_4–TiN–Y_2O_3 ceramics derived from chemically modified perhydropolysilazane, *J. Mater. Res.*, 1999, **14**, 4294–4301.

N(H) to promote electrocatalytic water oxidation in alkaline media, *Nanoscale Adv.*, 2022, **5**, 701–710.

28 Y. Iwamoto, K. Kikuta and S. Hirano, Synthesis of poly-titanosilazanes and conversion to Si_3N_4-TiN ceramics, *J. Ceram. Soc. Japan*, 2000, **108**, 350-356.

29 M. C. Bechelany, V. Proust, A. Lale, P. Miele, S. Malo, C. Gervais and S. Bernard, Nanocomposites through the Chemistry of Single-Source Precursors: Understanding the Role of Chemistry behind the Design of Monolith-Type Nanostructured Titanium Nitride/Silicon Nitride, *Chem. - A Eur. J.*, 2017, **23**, 832–845.

30 A. Lale, M. D. Mallmann, S. Tada, A. Bruma, S. Özkar, R. Kumar, M. Haneda, R. A. Francisco Machado, Y. Iwamoto, U. B. Demirci and S. Bernard, Highly active, robust and reusable micro-/mesoporous TiN/Si_3N_4 nanocomposite-based catalysts for clean energy: Understanding the key role of TiN nanoclusters and amorphous Si_3N_4 matrix in the performance of the catalyst system, *Appl. Catal. B Environ.*, 2020, **272**, 118975.

31 M. C. Bechelany, V. Proust, A. Lale, M. Balestrat, A. Brioude, C. Gervais, R. K. Nishihora and S. Bernard, From design to characterization of zirconium nitride/silicon nitride nanocomposites, *J. Eur. Ceram. Soc.*, 2022, **42**, 2135–2145.

32 M. Zaheer, G. Motz and R. Kempe, The generation of palladium silicide nanoalloy particles in a SiCN matrix and their catalytic applications, *J. Mater. Chem.*, 2011, **21**, 18825–18831.

33 S. Tada, M. D. Mallmann, H. Takagi, J. Iihama, N. Asakuma, T. Asaka, Y. Daiko, S. Honda, R. K. Nishihora, R. A. F. Machado, S. Bernard and Y. Iwamoto, Low temperature in situ formation of cobalt in silicon nitride toward functional nitride nanocomposites, *Chem. Commun.*, 2021, **57**, 2057–2060.

34 N. Asakuma, S. Tada, E. Kawaguchi, M. Terashima, S. Honda, R. K. Nishihora, P. Carles, S. Bernard and Y. Iwamoto, Mechanistic Investigation of the Formation of Nickel Nanocrystallites Embedded in Amorphous Silicon Nitride Nanocomposites, *Nanomaterials*, 2022, **12**, 1644.

35 M. Mallmann, R. Nishihora, E. Diz Acosta, P. Carles, N. Asakuma, S. Tada, Y. Iwamoto, U. Demirci, R. Machado and S. Bernard, From polysilazanes to highly micro-/mesoporous Si_3N_4 containing in situ immobilized Co or Ni-based nanoparticles, *Polymer*, 2023, **283**, 126215.

36 R. S. Mikhail, S. Brunauer and E. E. Bodor, Investigations of a complete pore structure analysis. I. Analysis of micropores, *J. Colloid Interface Sci.*, 1968, **26**, 45–53.

37 E. P. Barrett, L. G. Joyner and P. P. Halenda, The Determination of Pore Volume and Area Distributions in Porous Substances. I. Computations from Nitrogen Isotherms, *J. Am. Chem. Soc.*, 1951, **73**, 373–380.

38 D. Fonblanc, D. Lopez-Ferber, M. Wynn, A. Lale, A. Soleilhavoup, A. Leriche, Y. Iwamoto, F. Rossignol, C. Gervais and S. Bernard, Crosslinking chemistry of poly(vinylmethyl-*co*-methyl)silazanes toward low-temperature formable preceramic polymers as precursors of functional aluminum-modified Si-C-N ceramics, *Dalt. Trans.*, 2018, **47**, 14580–14593.

39 E. Zera, W. Nickel, S. Kaskel and G. D. Sorarù, Out-of-furnace oxidation of SiCN polymer-derived ceramic aerogel pyrolyzed at intermediate temperature (600-800°C), *J. Eur. Ceram. Soc.*, 2016, **36**, 423–428.

40 R. L. Puurunen, A. Root, S. Haukka, E. I. Iiskola, M. Lindblad and A. O. I. Krause, IR and NMR study of the chemisorption of ammonia on trimethylaluminum-modified silica, *J. Phys. Chem. B*, 2000, **104**, 6599–6609.

41 Q. Qu, L. Li, W. Bai, C. Yan and C. N. Cao, Effects of NaCl and NH_4Cl on the initial atmospheric corrosion of zinc, *Corros. Sci.*, 2005, **47**, 2832–2840.

42 C. Karakaya, S. Ricote, D. Albin, E. Sánchez-Cortezón, B. Linares-Zea and R. J. Kee, Thermogravimetric analysis of $InCl_3$ sublimation at atmospheric pressure, *Thermochim. Acta*, 2015, **622**, 55–63.

43 T. S. Lehmann, B. Blaschkowski and R. Niewa, Electrochemical Bulk Synthesis of Ternary Nitride Perovskites: Co_3InN and Ni_3InN, *Eur. J. Inorg. Chem.*, 2019, **2019**, 1709–1713.

44 H. Su, Y. Tang, H. Shen, H. Zhang, P. Guo, L. Gao, X. Zhao, X. Xu, S. Li and R. Zou, Insights into Antiperovskite $Ni_3In_{1-x}Cu_xN$ Multi-Crystalline Nanoplates and Bulk Cubic Particles as Efficient Electrocatalysts on Hydrogen Evolution Reaction, *Small*, 2022, **18**, 2105906.

45 S. Ilhom, A. Mohammad, D. Shukla, J. Grasso, B. G. Willis, A. K. Okyay and N. Biyikli, Elucidating the role of nitrogen plasma composition in the low-temperature self-limiting growth of indium nitride thin films, *RSC Adv.*, 2020, **10**, 27357–27368.

46 NIST X-ray Photoelectron Spectroscopy Database, NIST Standard Reference Database Number 20, National Institute of Standards and Technology, Gaithersburg MD, 20899 (2000), doi:10.18434/T4T88K

47 K. S. W. Sing, D. H. Everett, R. A. W. Haul, L. Moscou, R. A. Pierotti, J. Rouquerol and T. Siemieniewska, Reporting Physisorption Data for Gas/Solid Systems with Special Reference to the Determination of Surface Area and Porosity, *Pure Appl. Chem.*, 1985, **57**, 603–619.

48 M. Thommes, K. Kaneko, A. V. Neimark, J. P. Olivier, F. Rodriguez-Reinoso, J. Rouquerol and K. S. W. Sing, Physisorption of gases, with special reference to the evaluation of surface area and pore size distribution (IUPAC Technical Report), *Pure Appl. Chem.*, 2015, **87**, 1051–1069.

49 T. Konegger, C. Drechsel and H. Peterlik, In-situ small angle X-ray scattering (SAXS) – A versatile tool for clarifying the evolution of microporosity in polymer-derived ceramics, *Microporous Mesoporous Mater.*, 2021, **324**, 111268.

50 C. Schitco, M. S. Bazarjani, R. Riedel and A. Gurlo, NH_3-assisted synthesis of microporous silicon oxycarbonitride ceramics from preceramic polymers: A combined N_2 and CO_2 adsorption and small angle X-ray scattering study, *J. Mater. Chem. A*, 2015, **3**, 805–818.